Magnetospheric transmission function approach to disentangle primary from secondary cosmic ray fluxes in the penumbra region

P. Bobik,[1] G. Boella,[2,3] M. J. Boschini,[2,4] M. Gervasi,[2,3] D. Grandi,[2] K. Kudela,[1] S. Pensotti,[2,3] and P. G. Rancoita[2]

[1] The AMS-01 observations (in June 1998, on board the space shuttle orbiter Discovery) have shown the presence of primary (PCR) and secondary (SCR) cosmic rays (most of them protons) at a low Earth orbit (about 400 km altitude). The SCRs are mostly created in interactions with the atmosphere by fast PCRs and can be trapped or become reentrant albedo particles. Some of them seem to be sufficiently energetic to populate the ''penumbra region'' above the local geomagnetic cutoff rigidity. A backtracking procedure of simulated protons entering the AMS-01 spectrometer has provided the fraction of allowed (and hence forbidden) trajectories of PCRs. Consequently, it has allowed the determination of the so-called transmission function (TF) which is able to describe the properties of the PCR transport from the Earth's magnetopause (i.e., the primary spectrum at 1 AU) to the atmosphere and finally the fluxes of the PCRs in the ten geomagnetic regions for AMS-01 observations. In the penumbra regions, the observed spectra of the AMS-01 geomagnetic regions have been found to be larger than those predicted for the PCRs in the penumbra region by means of the TF, i.e., some SCRs (mainly reentrant albedo protons) are also found to populate the rigidity regions above the local geomagnetic cutoff rigidity. The fraction of the secondary to overall particle flux in the penumbra region increases gradually as the geomagnetic latitude increases.

1. Introduction

[2] Primary cosmic rays (PCRs) are particles reaching the Earth from outer space [see, e.g., *Smart and Shea*, 1985; *Longair*, 1992; *Schlickeiser*, 2001, and references therein]. However, the flux of PCRs is only a tiny fraction of the total particle flux observed at the Earth's surface or at low orbits (LOs) around the Earth. A dominant flux of secondary cosmic rays (SCRs) is generated by the interactions of PCRs with the atmosphere [e.g., see *Leroy and Rancoita* 2000, section 12; *Grieder*, 2001, chap. 1; *Leroy and Rancoita*, 2004, section 7.11, and references therein].

[3] The Sun is a major source of cosmic rays. The solar wind consists mostly of protons and electrons ejected from the solar corona and by solar flares. Solar wind and solar energetic particles have typically low energies (<100 MeV) and are prevented from reaching the Earth by the magnetosphere or absorbed in the upper atmosphere [see, e.g., *Toptygin*, 1985; *Smart and Shea*, 1989; *Gabriel*, 2000; *Lario and Decker*, 2001, and references therein]. The galactic cosmic rays (GCRs), mostly protons and α particles, have larger energies extending well above 100 MeV up to very high energies [see, e.g., *Simpson*, 1983; *Müller*, 1989; *Mewaldt*, 1994; *Stanev*, 2004, part 1, and references therein]. Most of them can pass through the magnetosphere and be observed at LOs.

[4] The AMS-01 experiment has flown on board the space shuttle in June 1998 and observed the flux of CRs at a LO with an altitude of ∼400 km [see, e.g., *Aguilar et al.*, 2002, and references therein]. The overall particle flux is a combination of PCRs and energetic SCRs (mainly electrons and protons [*Buenerd et al.*, 2000]). These latter, created by the interaction of high-energy CRs with the upper and middle atmosphere, can be trapped for a long time (i.e., several seconds) by the magnetic field near the Earth [*Vallarta*, 1961; *Roederer*, 1970]. Their flux depends on the flux and energy spectrum of the PCRs. At energies below a few GeV/nucleon, the solar modulation affects both

---

[1]Department of Space Physics, Institute of Experimental Physics, Kosice, Slovak Republic.
[2]Istituto Nazionale di Fisica Nucleare, Sezione di Milano, Milan, Italy.
[3]Department of Physics, University of Milano-Bicocca, Milan, Italy.
[4]Inter-University Consortium of Lombardy for Automatic Data Processing (CILEA) Segrate, Milan, Italy.

the flux and energy spectrum of the PCRs. Their flux is almost unaffected above about 8–10 GeV/nucleon [e.g., see *Smart and Shea*, 1989; *Gervasi et al.*, 1999, and references therein]. In addition, the Earth magnetosphere prevents the arrival of less energetic CRs at low magnetic latitudes and is related to the solar activity [e.g., see *Smart and Shea*, 1989; *Mewaldt*, 1994]. As a consequence, the observed flux of SCRs is also related to phenomena like the solar activity and magnetic storms. However, trapped and reentrant albedo energetic SCRs are always present and populate a radiation belt observed by AMS-01 (sometimes referred to as AMS radiation belt) at low altitude.

[5] While PCRs come from outside the magnetosphere, the SCRs originate in the Earth's atmosphere. They can be distinguished by reconstructing their trajectory (D. Grandi et al., private communication, 2005) from the observation point back to the border of the magnetosphere (if PCRs) or to the border of the atmosphere (if SCRs).

[6] The passage of the PCRs through the magnetosphere to the atmosphere is described by the so-called transmission function (TF) (see section 2). In this paper the TF has been determined by performing the reconstruction of the proton trajectories of a simulated spectrum, which reproduces the observed AMS-01 data (including both primary and secondary protons) on the shuttle orbiter Discovery [*Alcaraz et al.*, 2000a] and the AMS-01 primary proton spectrum at 1 AU [*Alcaraz et al.*, 2000b], i.e., at the Earth location inside the heliosphere but outside the magnetosphere. In addition, the reconstructed secondary proton spectra indicate the presence of a bump close to the energy region corresponding to the geomagnetic cutoff rigidity (i.e., within the so-called penumbra region), where primary protons are usually expected [*Cooke et al.*, 1991]; for a discussion about the local cutoff rigidity see, for instance, *Knecht and Shuman* [1985, section 6.2.3.1].

2. Transmission Function

[7] As mentioned above, the TF describes the properties of the PCR transport from the Earth magnetosphere boundary at 1 AU up to the observation point inside the magnetosphere. It depends on the PCR rigidity R, location of the observation point, solid angle, and pointing of the detecting instrument. Since the magnetic field does not change the particle rigidity but its direction, some of the PCRs might be prevented to access the observation point, while others (not pointing to it from outside the magnetosphere) can have access [see, e.g., *Störmer*, 1930; *Lemaitre and Vallarta*, 1933; *Lemaitre et al.*, 1935; *Lemaitre and Vallarta*, 1936a; *Lemaitre and Vallarta*, 1936b; *Vallarta*, 1949; *Fermi*, 1967; *Shea et al.*, 1968; *Smart et al.*, 1999, and references therein]. In addition for the same reason, the full flux of cosmic rays with rigidities R between $R - dR$ and $R + dR$ and within solid angle $d\Omega$ can be transported through the magnetosphere to the observation point, when is accessible (i.e., for allowed trajectories). As a consequence, flux in allowed range of rigidities is the same as that outside the magnetosphere [see, e.g., *Lemaitre and Vallarta*, 1933; *Vallarta*, 1949; *Fermi*, 1967]. In this latter region, it is commonly assumed that the flight directions of PCRs are isotropically distributed over the full solid angle. Recent AMS-01 observation data of the primary proton spectrum

[see, e.g., *Alcaraz et al.*, 2000b; *Aguilar et al.*, 2002] are in agreement with such an assumption.

[8] The overall effect of this transport is to relocate the space distribution of the PCRs within the magnetosphere depending on the location, direction, and particle rigidity outside the magnetosphere boundary. Thus the overall flux at the observation point varies and depends on the fraction of allowed among overall trajectories. The TF(R) is the differential probability for PCRs of rigidity R to be detected at the observation point [e.g., *Adams et al.*, 1991; *Boberg et al.*, 1995].

[9] In the present article, the TF is determined for the transport of PCRs to the AMS-01 spectrometer, located on board the shuttle orbiter during the STS-91 flight and for a PCR acceptance cone of 32° around the zenith [*Alcaraz et al.*, 2000a].

[10] The allowed trajectories [*Bobik et al.*, 2001] can be determined by the backtracking technique (see Appendix A), i.e., at fixed rigidity value R between $R - dR$ and $R + dR$ a particle entering the acceptance cone of the AMS-01 spectrometer is considered to be a PCR if its trajectory is backtracked up to the magnetopause. The backtracking procedure has demonstrated to be a powerful technique for obtaining the rigidity cutoff value and determining the allowed and forbidden cones of arrival directions as a function of the position in the Earth magnetosphere [see *Fluckiger et al.*, 1985; *Smart and Shea*, 1975; *Desorgher et al.*, 2003]. For the purpose of the calculations reported in the present article, the magnetosphere consists of an external geomagnetic field (described by the Tsyganenko96 model [*Tsyganenko*, 1995; *Tsyganenko and Stern*, 1996, and references therein] and an internal geomagnetic field described by the IGRF model, i.e., the DGRF 2000–2005 model [see *Barton*, 1997, and references therein], available at http://nssdc.gsfc.nasa.gov/space/model/magnetos/igrf.html). Thus the main novelty in the presented results is the presence of the external field (determined in the framework of the Tsyganenko96 model) in this type of calculation aimed at estimating the access of PCRs over the large area surrounding the Earth inside 51.6° latitude and an altitude of about 400 km, covered by the shuttle mission. The structure of the magnetosphere depends on the local time (t), especially for the external field model, and the geomagnetic activity (via the so-called K_p index). Thus since the distribution of the allowed trajectories depends on the magnetosphere structure, the TF is function of these parameters, i.e., $TF(R, t, K_p)$ (recently discussed, e.g., by *Kudela and Usoskin* [2004]). The penumbra region, where the particle rigidity is almost equal to the geomagnetic cutoff rigidity (R_c) at the observation location (e.g., D. Grandi et al., private communication, 2005), is a transition region, i.e., primary particles with rigidity much lower than R_c cannot reach this location (i.e., TF = 0) while with rigidity much larger than R_c are unaffected by the magnetic field (i.e., TF = 1).

2.1. Transmission Function and AMS-01 Data

[11] In the present article the TF has been determined for the 10 geomagnetic regions (see Table 1 and Figure 1), M, for which the AMS-01 data are available and is indicated by TF_M. As already mentioned, the observation period was June 1998. These regions are defined by means of the
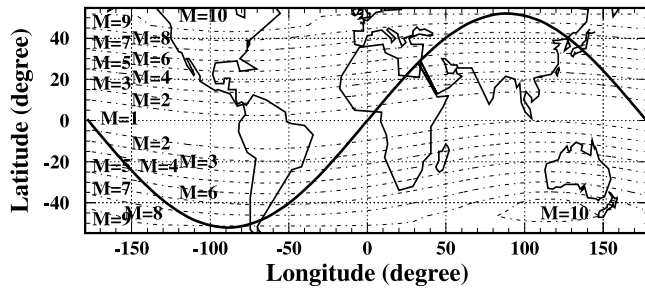
Figure 1. The ten geomagnetic regions (M) covered by AMS-01, defined in Table 1, are shown on the background of the Earth surface. A typical trajectory of AMS-01 detector on board the space shuttle, at an altitude of about 400 km, is also plotted. The space shuttle trajectory shifts with time and covers almost uniformly the Earth surface inside a geographic latitude $|\theta_{lat}| \leq 51.6°$.

corrected geomagnetic coordinates (CGM, http://nssdc.gsfc.nasa.gov/space/cgm/cgm.html). CGM coordinates (latitude and longitude) of a point in space are computed by tracing the DGRF/IGRF magnetic field line through the specified point to the dipole geomagnetic equator, then returning to the same altitude along the dipole field line and assigning the obtained dipole latitude and longitude as the CGM coordinates to the starting point.

[12] As discussed above, the TF_M requires the determination of the so-called allowed trajectories of the particles entering the AMS-01 spectrometer, following a backtracking procedure. The locations (3600) of the particles to be backtracked are distributed uniformly over a complete sphere surrounding the Earth at an altitude of 400 km and 78.9% of them are within the geographic latitudes of the orbits of the space shuttle, i.e., $|\theta_{lat}| \leq 51.6°$, excluding the South Atlantic anomaly region (i.e., the region with latitude between $-55°$ and $0°$ and with longitude between $-80°$ and $20°$).

[13] The particle directions (270) are isotropically distributed within the outward hemisphere and inside the 32° acceptance cone (around the local geocentric zenith) of the AMS-01 spectrometer. In addition, larger number of particle directions covering up to the full outward hemisphere have been backtracked to investigate the TF_M dependence on the acceptance cone. The TF_M has been computed for the same

Table 1. Geomagnetic Regions Covered by AMS-01 Measurements and Kinetic Energies Corresponding to the Dip for Each Geomagnetic Zone[a]

Region, M	CGM Latitude θ_M, rad	Kinetic Energy, GeV
1	$|\theta_M| \leq 0.2$	6.16
2	$0.2 \leq |\theta_M| \leq 0.3$	6.16
3	$0.3 \leq |\theta_M| \leq 0.4$	4.88
4	$0.4 \leq |\theta_M| \leq 0.5$	3.00
5	$0.5 \leq |\theta_M| \leq 0.6$	3.00
6	$0.6 \leq |\theta_M| \leq 0.7$	1.78
7	$0.7 \leq |\theta_M| \leq 0.8$	1.35
8	$0.8 \leq |\theta_M| \leq 0.9$	0.74
9	$0.9 \leq |\theta_M| \leq 1.0$	0.27
10	$|\theta_M| \geq 1.0$	0.07

[a]See *Alcaraz et al.* [2000a] and *Aguilar et al.* [2002]. The regions are defined using the corrected geomagnetic latitude (CGM).

31 rigidity intervals of the AMS-01 data [see *Aguilar et al.*, 2002, Table 4.5], i.e., the lowest rigidity value is about 0.37 GV and the largest is about 200 GV. To take into account the energy dependence of the proton flux, each energy interval has been subdivided in ten equally spaced subintervals. The subintervals have been weighted as function of their relative fluxes. For rigidities larger than 10 GV, the weights, $w_{b,s}$ (where $\sum_{s=1}^{10} w_{b,s} = 1$), are derived by the flux dependence on the proton rigidity R, i.e., $\phi(E) \propto R^{-2.78}$ [see, e.g., *Alcaraz et al.*, 2000b]. Below 10 GV, since the rigidity distribution becomes less steep, the subinterval flux variation has been interpolated using three adjacent rigidity bins. Within the acceptance cone of the AMS-01 spectrometer, about 2.3×10^8 particle trajectories have been reconstructed back to the magnetopause or to the atmosphere.

[14] For the ten geomagnetic regions, the TF_M has been averaged over all uniformly distributed locations:

$$TF_M(R_b) = \frac{\sum_{i_M} TF_M(R_b, i_M)}{\sum i_M}, \qquad (1)$$

where R_b is the particle rigidity in the bth rigidity interval of width ΔR_b, $TF_M(R_b, i_M)$ is the transmission function for the position i_M inside the geomagnetic region M, and Σi_M is the total number of locations for the same region. For the location i_M, $TF_M(R_b, i_M)$ is given by:

$$TF_M(R_b, i_M) = \sum_{s=1}^{10} w_{b,s} \frac{N_{all}^{i_M}(R_{b,s})}{N_{all}^{i_M}(R_{b,s}) + N_{forb}^{i_M}(R_{b,s})}, \qquad (2)$$

where $R_{b,s}$ is the mean rigidity of the sth subinterval of width $\Delta R_b/10$ for the bth rigidity bin, N_{allM}^i is the number of allowed trajectories, and the total (allowed and forbidden) number of computed trajectories is $N_{totalM}^i = N_{allM}^i + N_{forbM}^i$.

[15] In Figure 2, the TF_M for the ten different AMS-01 geomagnetic regions (given in Table 1) and during the STS-91 AMS-01 flight is shown as a function of the proton kinetic energy in GeV. As expected, toward the polar regions lower energy particles can reach the AMS-01 orbit through the magnetosphere.

[16] As mentioned above, the dependence of the TF_M on the acceptance cone of the AMS-01 spectrometer has been investigated. For instance, in Figure 3 the transmission
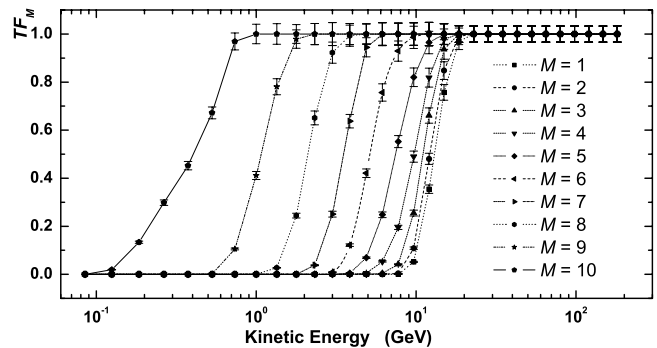

Figure 2. Transmission function (TF_M) evaluated for AMS-01 regions during the STS-91 mission flight time (June 1998) as a function of the proton kinetic energy in GeV. The lines are to guide the eye.
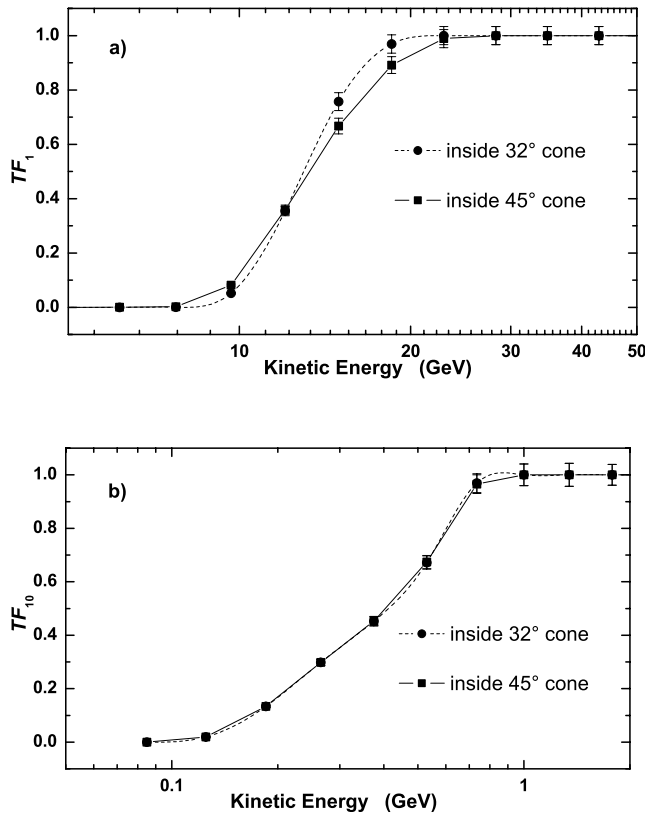
Figure 3. (a) TF_1 and (b) TF_{10} values as a function of the proton kinetic energy in GeV for detector acceptance cones of 32° and 45° around the local geocentric zenith. The lines are to guide the eye.

functions for the first and tenth geomagnetic regions are shown as functions of the proton kinetic energy for detector acceptance cones of 32° (i.e., the AMS-01 acceptance cone) and 45° (i.e., the expected AMS-02 acceptance cone) around the local geocentric zenith. The smaller the acceptance cone, the steeper the TF_M becomes. However, for geomagnetic regions beyond the fifth, the transmission functions become similar. The major contributions to the quoted errors for the transmission functions in Figures 2 and 3 account to about 1.4% for the uncertainty of the spectral index of the primary proton spectrum used in the subintervals, about 1% for AMS-01 altitude variation during the observation time and about 1.5% (in total) for the algorithm accuracy, treatment of the magnetic field model, and procedure of the speed optimization. Furthermore, although the TF_M has been computed for 8 June (1998) at 1000 UT, the TF_M does not vary by more than 0.1% during the AMS-01 observation duration at different day times for fixed geomagnetic condition (constant Dst = −22 nT, evaluated as average for full AMS-01 mission flight time).

3. Primary and Secondary Cosmic Ray Fluxes at AMS-01 Orbit

[17] Since particles approaching the Earth will experience a magnetic field similar to that of a dipole, they will be least affected (i.e., $R_c \sim 0$) when their directions are close the dipole axis and most on the geomagnetic equatorial plane

[e.g., see *Knecht and Shuman*, 1985; *Stanev*, 2004, chap. 5]. Thus the geomagnetic cutoff rigidity will be largest (lowest) in the first (tenth) geomagnetic region (e.g., see Figure 2).

[18] During the AMS-01 observation on board the STS-91 shuttle flight, the PCR flux per unit of solid angle at 1 AU ($\Phi^{1AU}(R_b)$) has been computed using data collected with an acceptance cone of 38° around the detector axis in three periods during which the shuttle attitude (within 1°) has allowed the AMS-01 spectrometer axis to point at 0°, 20° and 45° from the zenith [*Alcaraz et al.*, 2000b; *Aguilar et al.*, 2002].

[19] As already discussed, the AMS-01 observations have also provided the averaged fluxes per unit of solid angle ($\Phi_M^{exp}(R_b)$) for each geomagnetic region (i.e., for $1 \leq M \leq 10$ [e.g., see *Alcaraz et al.*, 2000a; *Aguilar et al.*, 2002]). The flux data in each region is statistically more limited than that of $\Phi^{1AU}(R_b)$ and, in addition, have been derived using an acceptance cone of 32° around the detector axis only when pointing at the zenith, i.e., further reducing the number of selected protons. However, in each geomagnetic region, for rigidities above the penumbra rigidity region (i.e., where $TF_M = 1$) the flux per unit of solid angle $\Phi_M^{exp}[R_b, TF_M(R_b) = 1]$ agrees, within the errors, with overall AMS-01 flux which we take as flux at 1 AU, i.e., with $\Phi^{1AU}[R_b, TF_M(R_b) = 1]$.

[20] Thus in the ten geomagnetic regions, the AMS-01 observed flux has been set (and indicated with $\Phi_{M,N}^{exp}(R_b)$) to that at 1 AU for rigidities larger than those of the penumbra region for each geomagnetic region:

$$\Phi_{M,N}^{exp}[R_b, TF_M(R_b) = 1] = \Phi^{1AU}[R_b, TF_M(R_b) = 1]. \quad (3)$$

For rigidities where $TF_M(R_b) = 0$, i.e., below the penumbra rigidities in each geomagnetic region, the observed fluxes have not been corrected, i.e.,

$$\Phi_{M,N}^{exp}[R_b, TF_M(R_b) = 0] = \Phi_M^{exp}[R_b, TF_M(R_b) = 0]. \quad (4)$$

Inside the penumbra regions for which $0 < TF_M(R_b) < 1$, the observed fluxes in each geomagnetic region M have been corrected to take into account (1) the effective detection of high-energy particles, i.e., the average difference among the observed flux and the corresponding flux at 1 AU in each rigidity bin above about 20.5 GeV of kinetic energy (these are energies large enough to neglect the geomagnetic dependence of the regions), and (2) the effective detection for each penumbra rigidity bin, i.e., the average difference among the observed flux and the corresponding flux at 1 AU in the same rigidity bin of the successive regions (with larger geomagnetic latitudes) where $TF_M = 1$. As an example, in Figure 4, the fluxes per units of solid angle $\Phi_{M,N}^{exp}(R_b)$ are shown for the geomagnetic regions 1, 4, 7, and 10 as functions of the proton kinetic energies. The errors accounting for the correction procedure have been added quadratically to the published errors for the observed fluxes from *Alcaraz et al.* [2000a].

[21] For the AMS-01 observations, the predicted PCR fluxes per unit of solid angle ($\Phi_M(R_b)$) are obtained by convolving the transmission function of each geomagnetic region (M) with the estimated AMS-01 flux $\Phi^{1AU}(R_b)$ (given in *Alcaraz et al.* [2000b]) at 1 AU, i.e., outside the
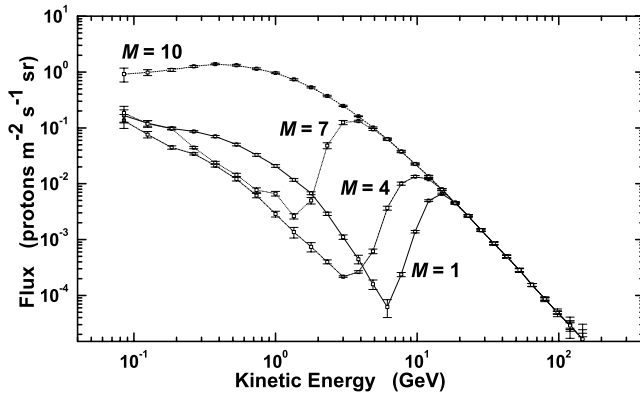
Figure 4. Normalized fluxes per units of solid angle $\Phi_{M,N}^{\exp}(R_b)$ (see text for explanation of the symbol) are shown for the geomagnetic regions $M = 1$, 4, 7, and 10 as functions of the proton kinetic energies. The lines are to guide the eye.

Figure 6. Fluxes per units of solid angle as a function of the proton kinetic energy for the fourth geomagnetic region: (open circle) $\Phi^{1AU}(R_b)$, (solid circle) $\Phi_4(R_b)$, and (square) $\Phi_4^s(R_b)$ (see text for explanation of the symbols). The lines are to guide the eye.

magnetosphere, as functions of the proton rigidity (R_b). Thus we have

$$\Phi_M(R_b) = \Phi^{1AU}(R_b)TF_M(R_b). \tag{5}$$

The SCR fluxes per unit of solid angle $\Phi_M^s(R_b)$ can be obtained as

$$\Phi_M^s(R_b) = \Phi_{M,N}^{\exp}(R_b) - \Phi_M(R_b). \tag{6}$$

As examples, in Figures 5–8 the fluxes per units of solid angle $\Phi^{1AU}(R_b)$, $\Phi_M(R_b)$, and $\Phi_M^s(R_b)$ are shown as functions of the proton kinetic energy for the first, fourth, seventh, and tenth geomagnetic region. The quoted errors for the fluxes $\Phi_M(R_b)$ and $\Phi_M^s(R_b)$ have been derived by the error propagations from those of the transmission functions $TF_M(R_b)$ and fluxes $\Phi^{1AU}(R_b)$ and $\Phi_{M,N}^{\exp}(R_b)$.

4. Results and Interpretation

[22] In section 3 the primary and secondary cosmic ray fluxes have been derived by means of the transmission
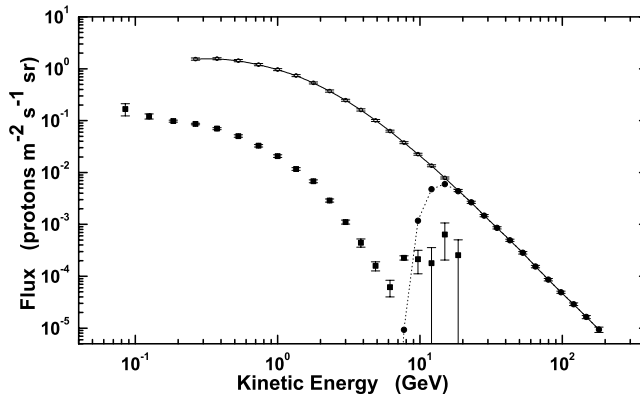
functions in each geomagnetic zone. It has been observed that in addition to the primary particles, secondary particles populate the penumbra region, i.e., approximately the energy region above the proton spectrum dip (e.g., see Figure 4), which depends, in turn, on the geomagnetic region (Table 1). Thus the geomagnetic cutoff energy is usually larger (and consequently the primary spectrum is steeper) than that corresponding to the dip position, as can be seen, for instance, by an inspection of the Figures 5–8. Besides, the position of the dip almost corresponds to the value at which the upward AMS-01 proton flux vanishes [*Alcaraz et al.*, 2000a; *Aguilar et al.*, 2002]. In the penumbra region, the fraction of secondary particles is lower than 6% in the first three geomagnetic regions, gradually increases up to about 16% in the geomagnetic region 7 and becomes larger than about 28% in the geomagnetic region 9. In the downward secondary fluxes (e.g., see, Figures 5–8), at first the high-energy part of the spectrum decreases because fewer and fewer particles are produced as the particle energy increases. These particles approach an almost isotropic distribution as the energy becomes lower and lower [see, e.g., *Treiman*, 1953]. For energies above the

Figure 5. Fluxes per units of solid angle as a function of the proton kinetic energy for the 1st geomagnetic region: (open circle) $\Phi^{1AU}(R_b)$, (solid circle) $\Phi_1(R_b)$, and (square) $\Phi_1^s(R_b)$ (see text for explanation of the symbols). The lines are to guide the eye.

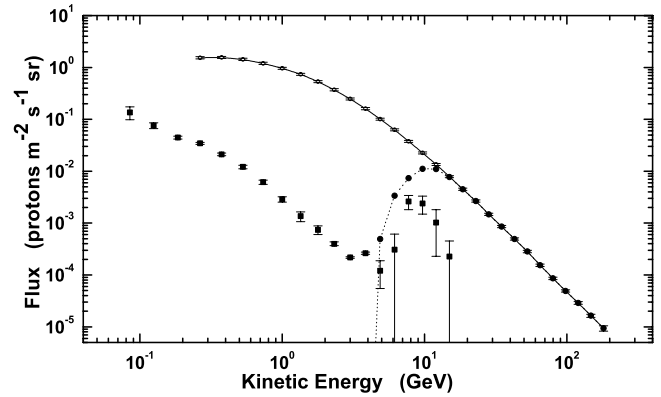**Figure 7.** Fluxes per units of solid angle as a function of the proton kinetic energy for the seventh geomagnetic region: (open circle) $\Phi^{1AU}(R_b)$, (solid circle) $\Phi_7(R_b)$, and (square) $\Phi_7^s(R_b)$ (see text for explanation of the symbols). The lines are to guide the eye.
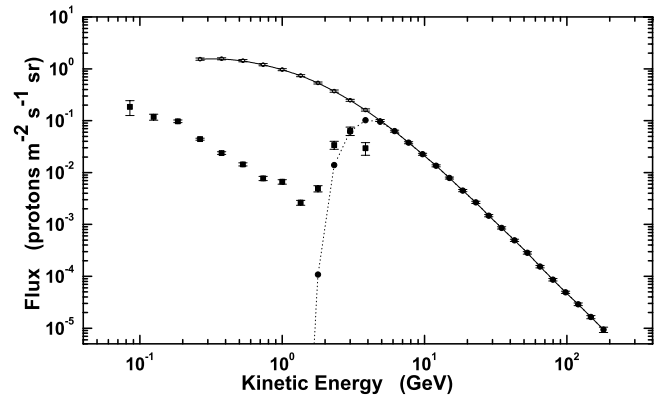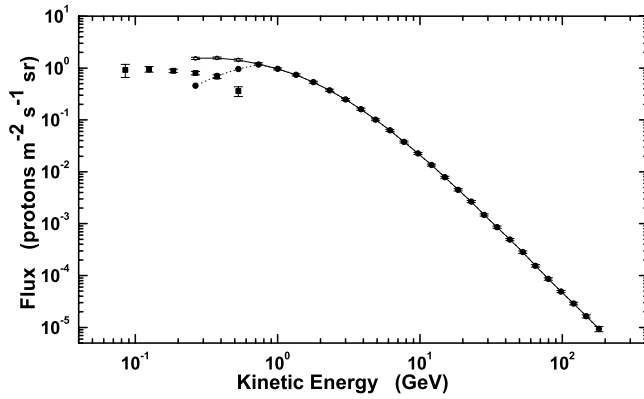
Figure 8. Fluxes per units of solid angle as a function of the proton kinetic energy for the tenth geomagnetic region: (circle) $\Phi^{1AU}(R_b)$, (solid) $\Phi_{10}(R_b)$, and (square) $\Phi_{10}^s(R_b)$ (see text for explanation of the symbols). The lines are to guide the eye.

dip, entering particles have large curvature radii (e.g., of order of 1000 km or greater) and come from more and more extended areas; thus the particle flux starts to increase again. However, it falls as the curvature radii are large enough to prevent the particles to reenter into the atmosphere. A reanalysis of the simulated data generated in the penumbra region has confirmed this interpretation. In the upward component this population cannot be present because of the Earth shadowing. Thus above the dip-energy, only (downward) reentrant albedo can be observed at the AMS-01 altitude.

[23] Since the models (IGRF and Tsyganenko96; see section 2 and Appendix A) of geomagnetic fields can be extrapolated for the next years, by means of the TFs we can estimate particle fluxes for future observations [see, e.g., *Bobik et al.*, 2005]. In fact the IGRF model is updated every 5 years (the next update, to be made available in the second half of the year 2005, is for years 2006–2010 (see http://nssdc.gsfc.nasa.gov/space/model/magnetos/igrf.html). While the Tsyganenko96 model depends on both solar conditions and period of the year: solar conditions, in turn, can be approximated by using the measurement of the last few solar cycles. Furthermore, the CR spectrum at 1 AU and modulated by the solar activity can also be estimated for coming years, for instance by means of the CREME96 model [*Tylka et al.*, 1997] when corrected to take into account the AMS-01 data [*Bobik et al.*, 2004].

[24] As discussed in section 2, the TF_M has been computed by applying a backtracking technique to identify the allowed trajectories from outside the magnetosphere up to the AMS-01 spectrometer. In this way the primary spectrum has been determined in each geomagnetic zone using the cosmic ray spectrum at 1 AU. In addition, it has to be noted that by reversing equation (5), it is possible to compute the cosmic spectrum once the primary spectrum of a geomagnetic zone has been observed. This procedure works only for rigidities larger than the local (i.e, that of the observation point) geomagnetic cutoff because below it we have $TF_M(R_b) = 0$. A similar computation can be applied to every measured spectrum of CRs inside the magnetosphere. In fact the transmission function can always be evaluated

when the experimental conditions (i.e., time, position, and attitude) are known.

5. Conclusions

[25] The AMS-01 observations (in June 1998, on board the space shuttle orbiter Discovery) have shown the presence of primary and secondary cosmic rays at a low Earth orbit, i.e., at an altitude of about 400 km. Most of these SCRs are trapped or fast reentrant albedo protons created in interactions with the atmosphere by fast incoming PCRs. Some secondary particles seem to be sufficiently energetic to populate the penumbra region above the local geomagnetic cutoff rigidity. A backtracking procedure of simulated protons entering the AMS-01 spectrometer has provided the fraction of allowed (and hence forbidden) trajectories of PCRs. Consequently, it has allowed to determine the so-called transmission function (TF) able to describe the transport properties of the PCRs to the space surrounding the Earth (at an altitude of about 400 km) from the upper limit of the geomagnetic field, i.e., the magnetopause located at 1 AU. The TF has finally allowed to determine the fluxes of the PCRs in the ten geomagnetic regions for AMS-01 observations.

[26] The observed spectra of the AMS-01 geomagnetic regions have been found to be larger that those predicted for the PCRs in the penumbra region by the TF procedure, i.e., some SCRs (mainly reentrant albedo protons) are also found to populate the spectrum above the local geomagnetic cutoff rigidity. The fraction of the secondary to overall particle flux in the penumbra region increases gradually to more than about 28% in the ninth geomagnetic region (i.e., for latitudes between 0.9 and 1.0 rad). Owing to Earth shadowing, this excess is only present in the downward proton flux.

[27] The models (IGRF and Tsyganenko96) of geomagnetic fields used to determine the TF can be extrapolated for the next years; as a consequence the TF can be derived for the same period of time. Furthermore, since the modulated CR spectrum at 1 AU can also be estimated for coming years, it becomes possible to predict particles fluxes at any observation location of future experiments inside the magnetosphere.

Appendix A: Particle Tracking Code

[28] The dynamics of charged particles in a magnetic field is defined by the Lorentz force:

$$m\frac{d\vec{v}}{dt} = Zq[\vec{v} \times \vec{B}], \qquad (A1)$$

where m is the relativistic mass of the particle, $\vec{v}$ is the velocity of the particle, $\vec{B}$ is the magnetic field, Z is the number of elementary charges, and q is the electron charge. The propagation equation remains unchanged when the charge sign and the velocity of the particle are simultaneously reversed. Therefore the trajectory of a particle incident on a detector surface can be evaluated by calculating the path of a particle with opposite charge generated from the detection point.

[29] The time step of calculation Δt is defined as a fraction of the gyration period τ. Every step the deflection

angle α in the particle trajectory is evaluated and compared with a threshold value $\alpha_\circ$. A procedure reduces the step until the condition $\alpha < \alpha_\circ$ is fulfilled. After several tests with particles backtracked starting from an altitude of $\sim$400 km, the code has been optimized in terms of speed and accuracy (see section 6.3). Typical values used in the calculation are $\alpha_\circ = 0.001$ rad; $\tau/\Delta t \simeq 8000$. An appropriate choice of these values prevents the code to repeat more than one time a check on the accuracy before passing to the next step of the trajectory calculation and reduce largely the CPU elapsed time.

[30] The differential equation (7) is solved numerically by means of the Runge-Kutta (RK) method of fourth order, which in literature is considered to provide an excellent balance of power, accuracy, and simplicity to program. The RK method of the sixth order has been tested but left after a comparison of the results in terms of precision of calculation (the difference is <0.5%) and the CPU time used ($\approx$20% more). A deep discussion on these tests is reported in section 6.3.2.

[31] The total magnetic field $\vec{B}$ is evaluated by adding the internal magnetic field model (the IGRF model) to the external field model (the model Tsyganenko96 (T96)): $\vec{B} = \vec{B}_{int} + \vec{B}_{ext}$. The Earth magnetopause (magp) is calculated using the Sibeck equation [*Sibeck et al.*, 1991] modified by Tsyganenko [*Tsyganenko*, 1995] for the solar wind effect. We have introduced an empirical magnetosphere boundary (magb) large 25 Earth radii ($R_e = 6371.2$ km) in the nightside region to avoid long calculations in the far tail. As internal boundary we have introduced a sphere at an altitude of 40 km (the 99% of the Earth atmosphere is contained inside this region).

[32] When the particle trajectory reaches the external boundaries the code evaluates the asymptotic direction and stops calculations. The main results of the calculation and outputs are the separation among allowed and forbidden trajectories, the final point of the trajectory, the asymptotic direction of the particle, the overall path length, and the time spent. The whole particle trajectory, step by step, can also be recorded. On the other hand the input data are the properties of the particle: mass, charge, and rigidity; and the setting of time and space at detection: position (i.e., geographic coordinates) and incoming direction, date, and time.

[33] Charged particles are generated at a fixed altitude ($\simeq$400 km), to simulate a space detector like AMS-01. They are backtracked in time until they reach one of the two boundaries: the Earth magnetopause or the atmosphere. In the first case the particles are considered as primary CR, otherwise secondaries.

A1. Internal Field

[34] The International Geomagnetic Reference Field (IGRF) model is the empirical representation of the Earth's magnetic field recommended for scientific use by the International Association of Geomagnetism and Aeronomy (IAGA) (see http://nssdc.gsfc.nasa.gov/space/model/magnetos/igrf.html). The IGRF model represents the main (core) field without external sources. It is a series of mathematical models describing the Earth's main field and its secular variation. Each model is built by using a set of spherical harmonic coefficients (called Gauss coefficients), g_n^m, h_n^m in a truncated series expansion of the internal geomagnetic potential:

$$V = R_e \sum_{n=1}^{N} \left[\frac{R_e}{r}\right]^{n+1} \times \sum_{m=0}^{n} \left[g_n^m \cos(m\phi) + h_n^m \sin(m\phi)\right] P_n^m(\cos\theta),$$

(A2)

where $R_e = 6371.2$ km is the mean radius of the Earth, while r, θ, ϕ are the geocentric spherical coordinates: r is the distance from the center of the Earth, ϕ is the longitude eastward from Greenwich, and θ is the colatitude. The $P_n^m(\cos\theta)$ are Schmidt quasi-normalized associated Legendre functions of degree n and order m ($n \geq 1$ and $m \leq n$).

[35] The IGRF models for the main field are truncated at $N = 10$ (120 coefficients). It represents a compromise adopted to produce well-determined main-field models while avoiding most of the contamination resulting from crustal sources. The coefficients of the main field are rounded to the nearest nT unit to reflect the limit of the resolution of the available data. The IGRF models for the secular variation are truncated at $N = 8$ and the coefficients are rounded at the nearest 0.1 nT/year. The IGRF model coefficients are based on all the available data sources including geomagnetic measurements from observatories, ships, aircrafts, and satellites. The IGRF model consists of a set of coefficients for the epochs starting from 1900 up to 2000, in steps of 5 years, and the first time derivatives of the coefficients for the time period 2000 to 2005. During the 5-year intervals between consecutive models, a linear interpolation is recommended.

A2. External Field

[36] The new model implemented by N. Tsyganenko (called Tsyganenko96 or T96 [see *Tsyganenko and Stern*, 1996]) calculates the external magnetic field in every point of the space out to 70 R_e. This field component is generated by charged particles circulating outside the solid Earth body. The external field component takes into account the interaction with the solar wind.

[37] The more complex morphology of the field and the variability of the solar activity make this one as the critical component. The model includes the following implementations: the position and the shape of the magnetopause, the boundary surface of the magnetosphere, is explicitly defined; the magnetic field of the region around the magnetopause is also considered; the interconnection of the Earth magnetosphere to the solar wind field at the boundary is taken into account too; furthermore the magnetic fields generated by the regions 1 and 2 of Birkeland currents, by the ring current, and by the tail current are added.

[38] As above mentioned, the analytical surface of the magnetopause is defined by Sibeck [see *Sibeck et al.*, 1991]: a half ellipsoid sunward, smoothly continuing as a cylinder down the far tail. The parameter controlling the size of the magnetopause is the solar wind pressure. The average value of the pressure is $\langle p_{dyn} \rangle \simeq 2$ nPa. It is assumed that under average solar wind conditions, the size and the shape of the magnetopause are fixed as the surface defined by Sibeck. Variations of the pressure around its average value produce self-similar compression/expansion of the boundary with a uniform spatial scaling of all the field sources. Distances are

scaling with the parameter k: $\vec{r} = k\langle\vec{r}\rangle$. The scaling factor k is defined as:

$$k = \left(\frac{p_{dyn}}{\langle p_{dyn} \rangle}\right)^{\beta}. \quad (A3)$$

The typical value of the power low index is $\beta \cong 0.14$. The parameters needed by this model are the Y and Z components of the interplanetary magnetic field (IMF in nT), the Dst index (in nT) (see the Dst web page, http://www.ngdc.noaa.gov/stp/GEOMAG/dst.html), and the solar wind pressure (in nPa).

[39] At the time we have performed our simulation a new model of external field has been completed and distributed by Tsyganenko (called T01 [see $Tsyganenko$, 2002]). The core is similar to the T96 model, but improvements have been added. We have tested the new subroutine and compared the results with the T96 model. Details of the test are described in section 6.3.3. The results of the two models present a relative difference $\varepsilon \simeq 0.007$, while the CPU elapsed time increased by a factor $\approx$10. Therefore we decided to keep for the simulation the T96 model.

A3. Accuracy of the Calculation

[40] Several sources of uncertainties contribute to the degradation of the accuracy of the results. Some of these are due to the structure, further errors can be added in the procedure of data reduction and analysis (i.e., the normalization procedure, data binning, etc.). The amount and the importance of the latter kind of uncertainties are depending on the particular analysis we are carried on and are discussed in the main text. Here we describe only the former set of error bars, proper of the tracking code.

A3.1. Processor and Operative System Accuracy

[41] We first have tested the angular precision of the code by evaluating the gyroradius calculation and generating particles with random rigidity at the Earth surface and tracked them up to the magp/magb. Then we retrace back these particles from the crossing point on magp/magb to the Earth. All the particles have reached back the Earth surface close to the original generation point. We studied the distribution of the final position and modified the code in order to get the maximum angular distance typically <0.5° both in latitude and longitude. This value corresponds to a linear jitter $r < 10^{-4} - 10^{-3}$ R_e.

[42] Then we have estimated the accuracy of the processor by checking the relative difference between the input rigidity of the particle and the rigidity computed at the final point of the trajectory, as obtained from the absolute value of the final velocity vector. This quantity (the velocity of the particle) is the main parameter of rigidity calculation and changes in every step: it is divided in components to get the gyroradius and then summed again to obtain the total velocity. We obtained that rigidity changes less than a part over 10^4 ($\delta R/R < 10^{-4}$). These uncertainties are due both to the discretization of the steps and the computer processing approximations.

A3.2. Algorithm Dependence

[43] In order to check the accuracy of the algorithm structure, we realized different codes without changing the standard NASA subroutines and maintaining the same main

structure, but (1) changing the algorithm procedure slightly and using the same RK version, (2) switching from the RK sixth order algorithm to the fourth order. The errors have been estimated on the base of the relative number of SCRs for one version of the code that became PCR with another version of the code and vice versa. This led to an estimation of the algorithm error of $\varepsilon \leq 10^{-3}$. The accuracy is estimated as the number of trajectories that are tagged differently by the two algorithms $N_{diff} = \Sigma n_{diff}$, relative to the total number of calculated trajectories N_{tot}, as shown in equation (10)

$$\varepsilon = \frac{\sum n_{diff}}{N_{tot}}. \quad (A4)$$

Here $n_{diff} = 1$ if the tag assigned by the two versions is different, while $n_{diff} = 0$ if the tag is the same.

A3.3. Accuracy of the Magnetic Field Model

[44] The evolution of magnetic field models forced us to evaluate the results using different subroutines. The internal field (the IGRF model) has survived a lot of tests for really long time. We kept the NASA subroutines (related to solar-terrestrial reference frames or to the motion of the geomagnetic poles for example) updated, but this did not introduce any measurable change in our results. Then we used different external field models, the Tsyganenko model of 1987 (T87) and that one of 1989 (T89), which are more simple to handle than both T96 and T01 (i.e., the most recent). We have tracked the particles covering the rigidity range 0.5–200 GV, geographical latitudes $-50° < \theta_{lat} < +50°$, and all geographical longitudes. The starting directions are inside a cone of 45° respect to the geocentric zenith. We have evaluated the output difference checking the number of allowed and forbidden trajectories in a test sample of particles, as described in section 6.3.2. We avoid to run the T87 that is obsolete, and evaluated T96 versus T89 and T01 both in precision and in speed. Between T96 and T89 we obtain a difference $\varepsilon \leq 5 \times 10^{-3}$. However, the T96 external model has the effect to slow down the code: the CPU time elapsed is 1.5 times longer than that for T89. However, an appropriate choice of the values of the parameters $\alpha_{\circ}$ and $\tau/\Delta t$ allows to obtain $\varepsilon \leq 10^{-4}$ and an extra CPU elapsed time of ∼0.6%. Comparing T96 and T01, the results show a difference $\varepsilon \simeq 7 \times 10^{-3}$, while the CPU elapsed time increased by a factor 9–10.

A3.4. Speed Versus Accuracy Optimization

[45] Owing to the complexity of the calculation and of the magnetic field model, we have also studied several strategies in order to reach the best speed performance. In particular we have tested the possibility to neglect the external field model, when not strictly necessary, and to use only the internal IGRF model. The intensity of the external field becomes comparable with the internal one at a distance greater than 4–5 R_e. Therefore we have chosen to reduce the frequency of calls to the external field subroutine: we calculated it for every step only at a distance larger than 4 R_e, while for a distance smaller than 2 R_e only the internal magnetic field is computed. In the intermediate region (2 < r/R_e <4) the number of calls to the external field is a fraction (1/2−1/5) of the calls to the internal field. The difference in the calculation is $\varepsilon < 10^{-4}$.

References

Adams, J. R., Jr., et al. (1991), The charge state of the anomalous component: Results from the trapped ions in space experiment, *Astrophys. J.*, *377*, 292.

Aguilar, M., et al. (2002), The Alpha Magnetic Spectrometer (AMS) on the International Space Station, part I, Results from the test flight on the space shuttle, *Phys. Rep.*, *366*, 331.

Alcaraz, J., et al. (2000a), Protons in near Earth orbit, *Phys. Lett. B*, *472*, 215.

Alcaraz, J., et al. (2000b), Cosmic protons, *Phys. Lett. B*, *490*, 27.

Barton, C. E. (1997), International Geomagnetic Reference Field: The seventh generation, *J. Geomagn., Geoelectr.,49*, 123.

Boberg, P. R., et al. (1995), Geomagnetic transmission of solar energetic protons during the geomagnetic disturbances of October 1989, *Geophys. Res. Lett.*, *22*, 1133.

Bobik, P., K. Kudela, and I. Usoskin (2001), Geomagnetic cutoff penumbra structure: Approach by transmissivity function, *Proc. Int. Conf. Cosmic Rays 27th*, 4056.

Bobik, P., M. Boschini, D. Grandi, M. Gervasi, E. Micelotta and P. G. Rancoita (2004), A normalization procedure for CREME96 spectra, in *Proccedings of the 8th ICATPP, 6–10 October 2003, Como, Italy*, p. 49, World Sci., Hackensack, N. J.

Bobik, P., M. Boschini, D. Grandi, M. Gervasi, E. Micelotta and P. G. Rancoita (2005), A back-tracing code to study the evolution of the magnetosphere transmission function for primary cosmic rays, in *The Inner Magnetosphere: Physics and Modeling, Geophys. Monogr. Ser.*, vol. 155, edited by T. I. Pulkkinen, N. A. Tsyganenko, and R. H. W. Friedel, p. 301, AGU, Washington, D. C.

Buenerd, M., et al. (2000), Origin of the high-energy proton component below the geomagnetic cutoff in near Earth orbit, *Phys. Lett. B*, *489*, 1.

Cooke, D. J., J. E. Humble, M. A. Shea, D. F. Smart, N. Lund, I. L. Rasmussen, B. Byrnak, P. Goret, and N. Petrou (1991), On cosmic-ray cut-off terminology, *Nuovo Cimento*, *14C*, 213.

Desorgher, L., E. O. Flückigher, M. R. Moser, and R. Bütikofer (2003), Geant4 application for simulating the propagation of cosmic rays through the Earth's magnetosphere, *Proc. Int. Conf. Cosmic Rays 28th*, 4281.

Fermi, E. (1967), *Nuclear Physics*, rev. ed., Univ. of Chicago Press, Chicago, Ill.

Flückigher, E. O., et al. (1985), Estimating the change in asymptotic direction due to secular changes in the geomagnetic field, *Proc. Int. Conf. Cosmic Rays 19th*, *5*, 336.

Gabriel, S. B. (2000), Cosmic rays and solar protons in the near Earth environment and their entry into the magnetosphere, paper presented at Workshop on the Utilization of a Future European Space Weather Service, ESTEC, Noordwijk, Netherlands.

Gervasi, M., P. G. Rancoita, and I. G. Usoskin (1999), Transport of galactic cosmic rays in the heliosphere: Stochastic simulation approach, *Proc. Int. Conf. Cosmic Rays 26th*, *7*, 69.

Grieder, K. F. (2001), *Cosmic Rays at Earth*, Elsevier, New York.

Knecht, D. J., and B. M. Shuman (1985), The geomagneic field, in *Handbook of Geophysics and the Space Environment*, edited by A. S. Jursa, chap. 4, Air Force Geophys. Lab., Hanscom Air Force Base, Mass.

Kudela, K., and I. G. Usoskin (2004), On magnetospheric transmissivity of cosmic rays, *Czech. J. Phys. B.*, *54*, 239.

Lario, D., and R. B. Decker (2001), Re-examination of the October 20, 1989 ESP event Proc, *Int. Conf. Cosmic Rays, 27th*, 3485.

Lemaitre, G., and M. S. Vallarta (1933), On Compton's latitude effect of cosmic radiation, *Phys. Rev.*, *43*, 37.

Lemaitre, G., and M. S. Vallarta (1936a), On the geomagnetic analysis of cosmic radiation, *Phys. Rev.*, *49*, 719.

Lemaitre, G., and M. S. Vallarta (1936b), On the allowed cone of cosmic radiation, *Phys. Rev.*, *50*, 493.

Lemaitre, G., M. S. Vallarta, and L. Bouckaert (1935), On the north-south asymmetry of cosmic radiation, *Phys. Rev.*, *47*, 434.

Leroy, C., and P. G. Rancoita (2000), Physics of cascading shower generation and propagation in matter: Principles of high-energy, ultrahigh-energy, and compensating calorimetry, *Rep. Progr. Phys.*, *63*, 505.

Leroy, C., and P. G. Rancoita (2004), *Principles of Radiation Interaction in Matter and Detection*, World Sci., Hackensack, N. J.

Longair, M. S. (1992), *High Energy Astrophysics*, 2nd ed., Cambridge Univ. Press, New York.

Mewaldt, R. A. (1994), Galactic cosmic ray composition and energy spectra, *Adv. Space Res.*, *14*, 737.

Müller, D. (1989), The composition of cosmic rays at high energies, *Adv. Space Res.*, *12*, 31.

Roederer, J. C. (1970), *Dynamics of Geomagnetically Trapped Radiation*, Springer, New York.

Schlickeiser, R. (2001), *Cosmic Ray Astrophysics*, Springer, New York.

Shea, M. A., D. F. Smart, and J. R. McCall (1968), A five degree by fifteen degree world grid of trajectory-determined vertical cutoff rigidities, *Can. J. Phys.*, *46*, S1098.

Sibeck, D. G., et al. (1991), Solar wind control of the magnetopause shape, location, and motion, *J. Geophys. Res.*, *96*, 5489.

Simpson, J. A. (1983), Elemental and isotopic composition of the galactic cosmic rays, *Annu. Rev. Nucl. Particle Sci.*, *33*, 323.

Smart, D. F., and M. A. Shea (1975), *Cosmic-Ray Penumbral Effects for Selected Balloon Launching Locations*, U. S. Air Force, Washington, D. C.

Smart, D. F., and M. A. Shea (1985), Galactic cosmic radiation and solar energetic particles, in *Handbook of Geophysics and the Space Environment*, edited by A. S. Jursa, chap. 6, Air Force Geophys. Lab., Hanscom Air Force Base, Mass.

Smart, D. F., and M. A. Shea (1989), Solar proton events during the past three solar cycles, *J. Spacecr. Rockets*, *26*, 403.

Smart, D. F., M. A. Shea, E. O. Flückiger, A. J. Tylka, and P. R. Boberg (1999), Changes in calculated vertical cutoff rigidities at the altitude of the International Space Station as a function of geomagnetic activity, *Proc. Int. Conf. Cosmic Rays 26th*, *7*, 337.

Stanev, T. (2004), *High Energy Cosmic Rays*, Springer, New York.

Störmer, K. (1930), Periodische Elektronenbahnen im Felde eines Elementarmagneten und ihre Anwendung auf Brüches Modellversuche und auf Eschenhagens Elementarwellen des Erdmagnetismus. Mit 32 Abbildungen, *Z. Astrophys.*, *1*, 237.

Toptygin, I. N. (1985), Cosmic rays in interplanetary magnetic fields, in *Cosmic Rays in Interplanetary Magnetic Fields*, chap. 3, Springer, New York.

Treiman, S. B. (1953), The cosmic ray albedo, *Phys. Rev.*, *91*, 957.

Tsyganenko, N. A. (1995), Modeling the Earth's magnetospheric magnetic field confined within a realistic magnetopause, *J. Geophys. Res.*, *100*, 5599.

Tsyganenko, N. A. (2002), A model of the near magnetosphere with a dawn-dusk asymmetry: 1. Mathematical structure, *J. Geophys. Res.*, *107*(A8), 1179, doi:10.1029/2001JA000219.

Tsyganenko, N. A., and D. P. Stern (1996), Modeling the global magnetic field of the large-scale Birkeland current systems, *J. Geophys. Res.*, *101*, 27,187.

Tylka, A. J., J. H. Adams, P. R. Boberg, B. Brownstein, W. F. Dietrich, E. O. Flückigher, E. L. Petersen, M. A. Shea, D. F. Smart, and E. C. Smith (1997), CREME96: A revision of the cosmic ray effects on microelectronics code, *IEEE Trans. Nucl. Sci.*, *44*, 2150.

Vallarta, M. S. (1949), On the energy of cosmic radiation allowed by the Earth's magnetic field, *Phys. Rev.*, *74*, 1837.

Vallarta, M. S. (1961), Theory of geomagnetic effects of cosmic radiation, in *Handbuch der Physik*, vol. XLVI/I, Springer, New York.

_____

P. Bobik and K. Kudela, Department of Space Physics, Institute of Experimental Physics, Watsonova 47, 040 01, Kosice, Slovak Republic. (pavol.bobik@mib.infn.it; kkudela@upjs.sk)

G. Boella, M. Gervasi, D. Grandi, S. Pensotti, and P. G. Rancoita, Istituto Nazionale di Fisica Nucleare, Sezione di Milano, Piazza della Scienza 3, I-20126, Milan, Italy. (giuliano.boella@mib.infn.it; massimo.gervasi@mib.infn.it; davide.grandi@mib.infn.it; simonetta.pensotti@mib.infn.it; piergiorgio.rancoita@mib.infn.it)

M. J. Boschini, Inter-University Consortium of Lombardy for Automatic Data Processing (CILEA), Via R. Sanzio, 4, I-20090, Segrate (M), Italy. (matteo.boschini@mib.infn.it)